Cement and Concrete Research 52 (2013) 31–37

Contents lists available at SciVerse ScienceDirect

Cement and Concrete Research

journal homepage: http://ees.elsevier.com/CEMCON/default.asp

On the nature of structural disorder in calcium silicate hydrates with a calcium/silicon ratio similar to tobermorite

Sylvain Grangeon [a,*], Francis Claret [a], Catherine Lerouge [a], Fabienne Warmont [b], Tsutomu Sato [c], Sohtaro Anraku [c], Chiya Numako [d], Yannick Linard [e], Bruno Lanson [f]

[a] BRGM, 3, Avenue Claude Guillemin, 45060 Orléans Cedex 2, France
[b] CRMD, UMR 6619 – CNRS, 1b rue de la férollerie, 45071 Orléans Cedex 2, France
[c] Laboratory of Environmental Geology, Research Group of Geoenvironmental/Engineering Division of Solid Waste, Resources and Geoenvironmental/Engineering Graduate School of Engineering, Hokkaido University, Kita 13 Nishi 8, Sapporo 060-8628, Japan
[d] Faculty of Integrated Arts and Sciences, The University of Tokushima, 1-1, Minami-Josanjima, Tokushima, 770-8502, Japan
[e] ANDRA, Centre de Meuse/Haute Marne, 55290 Bure, France
[f] ISTerre, Grenoble University, CNRS, F-38041 Grenoble, France

ARTICLE INFO

Article history:
Received 18 September 2012
Accepted 3 May 2013
Available online xxxx

Keywords:
Calcium–silicate–hydrate (C – S – H)(B)
Crystal structure(B)
X-ray diffraction(B)
Spectroscopy(B)
TEM(B)

ABSTRACT

Four calcium silicate hydrates (C – S – H) with structural calcium/silicon (Ca/Si) ratios ranging from 0.82 ± 0.02 to 0.87 ± 0.02 were synthesized at room temperature, 50, 80, and 110 °C. Their structure was elucidated by collating information from electron probe micro-analysis, transmission electron microscopy, extended X-ray absorption fine structure spectroscopy, and powder X-ray diffraction (XRD). A modeling approach specific to defective minerals was used because sample turbostratism prevented analysis using usual XRD refinement techniques (e.g. Rietveld analysis). It is shown that C – S – H with Ca/Si ratio of ~0.8 are structurally similar to nano-crystalline turbostratic tobermorite, a naturally occurring mineral. Their structure thus consists of sheets of calcium atoms in 7-fold coordination, covered by ribbons of silicon tetrahedra with a dreierketten (wollastonite-like) organization. In these silicate ribbons, 0.42 Si per bridging tetrahedron are missing. Random stacking faults occur systematically between successive layers (turbostratic stacking). Layer-to-layer distance is equal to 11.34 Å. Crystallites have a mean size of 10 nm in the **a**–**b** plane, and a mean number of 2.6–2.9 layers stacked coherently along the c^* axis.

1. Introduction

In cement pastes, hydration of Ca_2SiO_4 and Ca_3SiO_5, two anhydrous calcium silicates accounting for more than two thirds of the Portland cement weight, leads to cryptocrystalline synthetic products named calcium silicate hydrates (C – S – H) with no known natural equivalent [1–3]. Their chemical composition is extremely variable. In particular, their structural Ca/Si ratio varies from ~0.6 to ~2.3, with eventually spatial heterogeneity within a given cement paste [4], in which C – S – H aggregates are called C – S – H gel, and refer to a material containing a mixture of individual C – S – H phases developing a rigid network structure [5,6]. In neat Portland cement, only the C – S – H with highest Ca/Si ratio (>~1.5) are observed, whereas C – S – H with the whole compositional range may exist in cement pastes containing fly ash, metakaolin or silica fume, for example [7,8]. The Ca/Si ratio of C – S – H influences both mechanical [3,9] and chemical properties such as equilibrium pH or aqueous Si and Ca concentrations [10–12]. Despite the variability of Ca/Si ratio in C – S – H, thermodynamic solubility models such as those developed by Blanc and coworkers and Stronach and Glasser only require three phases (with Ca/Si equal to 0.8, 1.1 or 1.2, depending on the authors, and 1.6 or 1.8) to reproduce the whole compositional range of water in equilibrium with C – S – H [11,13,14]. Such models were elaborated from least-square refinement of experimental solubility data and, although efficient, lack a sound crystallographic basis that would allow both a more efficient prediction of thermodynamic properties, an easier prediction of the properties of phases with intermediate chemical composition, and comparison with crystalline minerals such as tobermorite or jennite.

Because their X-ray diffraction fingerprint consists in a few broad diffraction bands, C – S – H are often described as X-ray amorphous, with no long-range order, and only a few studies investigated C – S – H crystal structure with X-ray diffraction (XRD) and the Rietveld method [5,15]. Although these studies represent a valuable contribution to the understanding of C – S – H crystal structure, they were either applied to structures with a 3D order assumed to be similar to that of C – S – H [5], or were limited by the intrinsic disorder in C – S – H that results in broad and asymmetric diffraction peaks. Anisotropic line broadening and shift of $hk0$ reflections with $h + k =$

---

* Corresponding author. Tel.: +33 2 386 435 11; fax: +33 2 386 430 62.
E-mail address: S.Grangeon@brgm.fr (S. Grangeon).

0008-8846/$ – see front matter © 2013 Elsevier Ltd. All rights reserved.
http://dx.doi.org/10.1016/j.cemconres.2013.05.007

4*n* were thus introduced by Renaudin and coworkers [15] to reduce the intensity of *hkl* reflections relative to *hk*0 and to fit the angular position of *hk*0 reflections. This approach was not sufficient to eliminate totally *hkl* reflections, in contrast to XRD data. In addition, the parameters introduced have no clear physical meaning, and the nature of structural disorder in C–S–H cannot be determined. Finally, in the cited study, interpretation is complicated by the variable degree of structural disorder, depending on the C–S–H Ca/Si ratio: only *hk* bands are visible on the XRD pattern obtained from the C–S–H sample with low Ca/Si (0.8), whereas a *hkl* Bragg peak is visible at ~30.2 °2θ CuKα for the sample with high Ca/Si (1.7). To circumvent the difficulties related to long-range disorder, short- and medium-range order in C–S–H has been extensively investigated with a variety of physical methods including transmission electron microscopy [TEM—16], Fourier-transform infrared [FTIR—17] and Raman spectroscopies [Raman—18], ^{29}Si, ^{17}O and more recently ^{43}Ca nuclear magnetic resonance spectroscopy [NMR—e.g. 19–21], extended X-ray absorption fine structure spectrometry [EXAFS—22], small-angle neutron scattering [SANS—23,24] and synchrotron-based pair distribution function [PDF—25]. These studies allowed proposing or support different structure models for C–S–H [e.g. 19,26–29], which were recently reviewed [30]. Richardson [30] demonstrated that structure models describe C–S–H as a mixture of minerals tobermorite and/or jennite (depending on the Ca/Si ratio) with contrasting degrees of structural disorder. When Ca/Si matches that of tobermorite, C–S–H structure is thought to be close to this model mineral. In the literature, three main varieties of tobermorite have been differentiated from their layer-to-layer distance [9,11 or 14 Å—31–34]. In all of them, the layer consists of sheets of calcium in 7-fold coordination, sandwiched by Si tetrahedra ribbons linked as in wollastonite and named “drierketten”. The interlayer contains Ca and water molecules in variable amounts.

Despite this abundance of structural studies, the structure of C–S–H is not known in detail [35,36]. The present study thus aims at determining this structure, focusing on four synthetic C–S–H with a Ca/Si ratio ranging from 0.82 ± 0.02 to 0.87 ± 0.02, consistent with that of natural and synthetic tobermorite [37]. C–S–H were synthesized at temperatures ranging from room temperature to 110 °C to assess the potential influence of this parameter on structural (dis-)order, as reported earlier [38] for air-dried samples. Crystal chemistry of C–S–H was determined by combining electron probe micro-analysis (EPMA), TEM, EXAFS spectroscopy and powder X-ray diffraction. XRD patterns were successfully modeled, thus providing meaningful and accurate structural information, including structure defects, despite the weak modulation of the profiles. A full structure model is thus proposed for C–S–H with Ca/Si ratio equal to ~0.8.

2. Material and methods

2.1. Synthesis of samples

Synthetic C–S–H samples and tobermorite were synthesized under soft hydrothermal conditions from a mixture of 202.3 g $Ca(OH)_2$ and 197.7 g amorphous silica in 1.2 L of CO_2 free and de-ionized water (resistivity = 18.2 MΩ·cm). C–S–H experiments were run at 0.14 MPa for 72, 12, 12, and 3.5 hours at room temperature, 50 °C, 80 °C and 110 °C, respectively. Tobermorite was synthesized for 8.5 hours at 1.0 MPa and 180 °C. All suspensions were stirred at 60 rpm during the synthesis. C–S–H samples are labeled CSH_X, where X stands for the synthesis temperature (RT—room temperature, 50, 80, or 110 °C).

2.2. Electron probe micro-analysis

Structural Ca/Si ratio was determined by EPMA to avoid possible contamination by unreacted material or accessory newly formed phases, although such phases were not observed. Analyses were performed on polished thin sections with a Cameca SX50 probe using a 15 kV acceleration voltage, a 12 nA beam current, and a 1–2 μm wide beam. Prior to analysis, samples were sputter-coated with a 10–20 nm thick carbon (Edwards Auto 306). Al, Ba, Ca, Fe, K, Mg, Na, Si and Sr elements were analyzed from their Kα emission lines (Lα for Ba and Sr). Ca, K, and Ba were analyzed using a PET (Pentaerythritol) crystal, Fe with a LiF (Lithium fluoride) crystal, and Al, Mg, Na, Si and Sr with a TlAP (thallium acid phthalate) crystal. Standards included both natural minerals and synthetic oxides: albite ($NaAlSi_3O_8$) for Na and Si, synthetic Al_2O_3 for Al, baryte ($BaSO_4$) for Ba, synthetic Fe_2O_3 for Fe, synthetic MgO for Mg, orthoclase ($KAlSi_3O_8$) for K, celestite ($SrSO_4$) for Sr and wollastonite ($CaSiO_3$) for Ca. Counting times were 10 s for Al, Ca, Fe, K, Mg, Na, Si, and 60 s for Ba and Sr. Matrix effects were corrected with a ZAF program [39].

2.3. Extended X-ray absorption fine structure (EXAFS) spectroscopy

Ca K-edge EXAFS spectra were measured in transmission mode on beamlines 9A and 12C at the Photon Factory, KEK (Tsukuba, Japan). Synchrotron radiation from the 2.5 GeV storage ring was monochromatized with Si(111) double crystal monochromator, energy being calibrated with a Cu foil. The incident beam was collimated to 1.0 × 1.0 mm^2 with slits. Powder specimens were kept in plastic sample holders for data collection. Data were post-processed using home-made software and simulated using Artemis [40], included in the Ifeffit program suite [41], using the single scattering approximation. Theoretical phases and amplitudes were generated using Atoms [42] and Feff [43], using tobermorite MDO2 from Urals [34] as a template. Fourier transforms were performed using a Kaiser–Bessel window with $\tau = 3$. Amplitude reduction factor (S_0^2) was 0.7 [22].

2.4. Transmission electron microscopy

Only CSH_RT was observed on a Philips CM-20 microscope operated at 200 kV as all prepared C–S–H were chemically and structurally (see below) similar. C–S–H was first dispersed in ultra-pure ethanol using ultrasonic bath and then deposited on carbon-coated copper grids. Several experimental difficulties hampered observations: first, crystals, and especially the smallest ones, tended to aggregate thus making it virtually impossible to observe isolated single crystals. Second, C–S–H crystals had a very limited lifetime under the beam: the distance between interference fringes would decrease within a few seconds (likely as a result of dehydration) before melting yielding amorphous product. As a result, analyses of a specific crystal could not be repeated, and single information could be obtained per crystal (either low-resolution image, high-resolution interference fringe image or diffraction pattern).

2.5. Powder X-ray diffraction (XRD)

XRD patterns were collected using a Rigaku RINT-2000 diffractometer using Cu Kα radiation (λ = 1.5418 Å). Intensities were recorded over the 2–70 °2θ range in step mode, at a scanning rate of 1 °2θ per minute. As described hereafter, C–S–H XRD patterns are typical of turbostratic structures lacking *hkl* reflections and exhibiting only basal reflections and *hk* bands. This specific diffraction signature, first described for carbon blacks [44], arises from the systematic presence of random translations and/or rotations between adjacent layers, and thus from the absence of three dimensional periodicity. In this case, the algorithm developed by Plançon [45,46] and based on the numerical formalism described by Drits and Tchoubar [47] is especially relevant. This approach has been described elsewhere [see for example 48], and successfully applied to determine the structure of turbostratic phyllosilicates and phyllomanganates [48–52]. The trial-and-error optimization strategy does not allow the calculation of a correlation matrix, and errors on adjusted parameters cannot be mathematically calculated. The precision on structural parameters will thus be assessed from sensitivity tests. In the present study the inability to obtain a correlation matrix has limited implication, as very few parameters of the initial 11 Å tobermorite structure model were refined. In particular, atomic coordinates were not refined. Simulations were carried out in two steps: first, the layer and interlayer structure (**a** and **b** unit-cell parameters, site occupancies and abundance of stacking faults) was determined from the simulation of *hk* bands. Then, 00*l* reflections were simulated to determine the mean number of coherently stacked layers, assuming a log-normal distribution. Simulation quality was assessed with the common R_{wp}, R_{exp}, and Goodness of Fit [GoF $= (R_{wp} / R_{exp})^2$] parameters [53].

3. Results and discussion

3.1. Synthetic tobermorite and C–S–H chemical composition

About 50 EPMA analyses of different crystal aggregates were performed on tobermorite and on the four C–S–H samples. Al, Ba, Fe, K, Mg, Na, and Sr contents were always below or comparable to the detection limit (~200 µg g^{-1} for Al, 426 µg g^{-1} for K, 379 µg g^{-1} for Fe, 705 µg g^{-1} for Mn and 259 µg g^{-1} for Mg). Average Ca/Si atomic ratio based on analyses of n independent crystal aggregates was 0.82 ± 0.02 ($n = 56$) for tobermorite, 0.84 ± 0.03 ($n = 48$) for CSH_RT, 0.87 ± 0.02 ($n = 47$) for CSH_50, 0.86 ± 0.01 ($n = 50$) for CSH_80 and 0.84 ± 0.02 ($n = 49$) for CSH_110. The absence of analyses of unreacted product and the good reproducibility of the Ca/Si confirm the purity of tobermorite and of the four C–S–H samples. Note that repeated analyses of the Ca/Si ratio on a wollastonite standard were performed for quality insurance, and always let to the theoretical value of 1.

3.2. EXAFS data analysis

k^3-weighted EXAFS spectra of the four C–S–H are statistically indistinguishable (Fig. 1), which indicates that synthesis temperature does not impact C–S–H local structure over the temperature range tested. Comparison between tobermorite and C–S–H spectra reveals no significant difference. Amplitude and frequency are equal, thus suggesting similar local environment around Ca in both C–S–H and tobermorite. C–S–H spectra being identical, and to improve signal/noise ratio, simulations were performed on an average $k^3\chi(k)$ EXAFS C–S–H spectrum (CSH_averaged) filtered over the 1.2–3.4 Å $R + \Delta R$ range. The best simulation (Fig. 2, Table 1) was obtained for a four-shell model with two oxygen shells at 2.36 Å and 2.51 Å and two silicon shells at 3.11 Å and 3.41 Å (Table 1) and converged to a residual R-factor value of 0.011. It consists of 8 independent variables and thus meets the Nyquist criterion, the number of independent points [$(2\ \Delta k\ \Delta R) / \pi$] being larger than 12. Reducing the number of oxygen atomic shells to one led to lower quality, although acceptable, simulation (R-factor = 0.016), with 6.8 ± 0.9 oxygen atoms at 2.39 ± 0.01 Å and $\sigma^2 = 0.12 \pm 0.02$ Å^2. These values are similar to published Ca–K EXAFS refinements [22] and are consistent, within error, with tobermorite crystallographic number of oxygen neighbors (7 with layer Ca–O distance < 3 Å [34]). This model can however be improved, as the high value of Debye–Waller factor challenges the assumption of a Gaussian atomic distribution around absorbing Ca [54,55]. The existence of two distinct shells, whose total number of oxygen atoms was constrained to 7 so as to reduce the number of adjusted parameters, is thus favored. The simulated k range allows the ~0.15 Å ΔR resolution [$\pi / (2\ k_{max})$] required to distinguish the two oxygen shells. As for oxygen, reducing the number of Si atomic shells to one led to equivalent fit quality parameter (R-factor = 0.012) and to unrealistically high Debye–Waller value ($\sigma^2 > 0.01$ Å^2). During the refinement the number of Si atoms in each shell had to be constrained to tobermorite crystallographic value to prevent the refinement algorithm from reaching a solution with unrealistically high Debye–Waller factors ($\sigma^2 = 0.012$ Å^2) despite relative contents of the two Si shells similar to the optimum model ($CN_{Si1}/CN_{Si2} = 1.73/3.5 = 0.5$, compared to tobermorite crystallographic value of 1/2). Finally, freeing the coordination number from the Ca–Si1 shell to account for a possible decrease in the occupation of the bridging tetrahedron led to a solution where the occupancy of Si1 was equal to 1 within uncertainties ($CN_{Si1} = 0.7 \pm 0.5$), all other parameters being similar to the model with Si1 occupancy set to 1 ($CN_{O1} = 4.3 \pm 1.3$; $\sigma^2_O = 0.005 \pm 0.004$; $\sigma^2_{Si} = 0.006 \pm 0.003$). The model with the lower amount of free parameters was preferred.

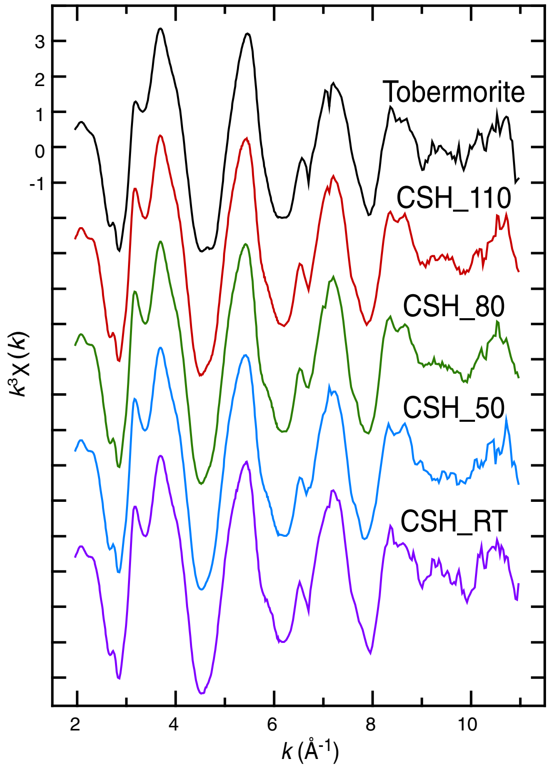

Fig. 1. k^3-weighted EXAFS spectra of tobermorite and C–S–H samples synthesized at 110 °C, 80 °C, 50 °C and room temperature, from top to bottom.

Analysis of our data shows that interlayer calcium does not modulate the EXAFS signal to a measurable extent. This certainly results from its low abundance (11% of total calcium, see below) as compared to layer calcium, and from intrinsic positional disorder of interlayer species.

3.3. Size and shape of C–S–H crystals and lattice parameters estimation using TEM

Under the TEM, crystals had platelet morphology, with interference fringes parallel to the platelets. Such observation supports the hypothesis of a layered material, with limited extension along c^*. Crystal aggregation prevented a statistically robust evaluation of the mean crystal size. Visual observation (Fig. 3a) indicates however that most of the crystals have sizes with their large dimension in the layer plane ranging from 10 to 50 nm. Larger crystals, with dimensions within the layer plane up to ~200 nm were regularly observed, but their proportion is minor.

Smallest crystals have no specific morphology, whereas larger crystals have well defined edges and angles (Fig. 3b). With the **a**–**b** plane parallel to the interference fringes resulting from layer stacking,

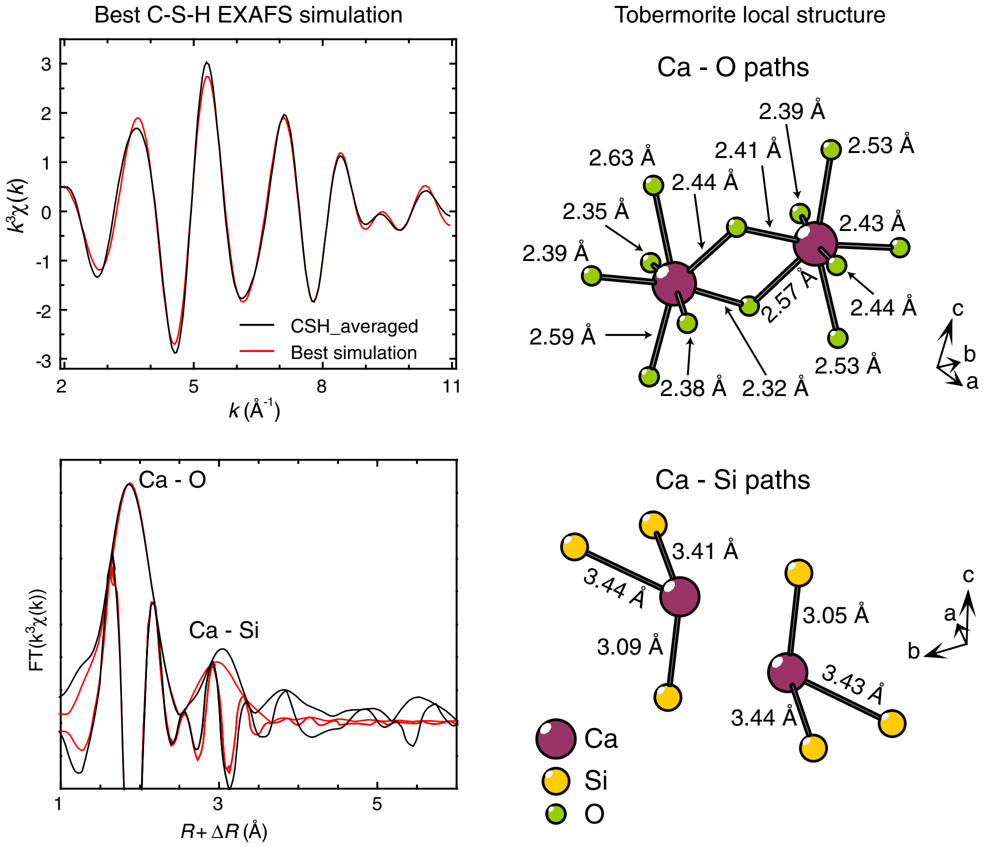

Fig. 2. Left: data (black line) and best simulation (red line) of the average k^3-weighted CSH_averaged EXAFS spectrum filtered over the 1.2–3.4 Å $R + \Delta R$ range (top) and comparison between the Fourier transforms of best simulation and of CSH_averaged spectra (bottom). Right: sketch of tobermorite layer structure with Ca–O bonds up to 3 Å (top) and Ca–Si bonds up to 3.5 Å (bottom). (For interpretation of the references to color in this figure legend, the reader is referred to the web version of this article.)

the angle between **a** and **b** is equal to ~120° (or ~60°), as shown on Fig. 3b, consistent with that of tobermorite (123.18° for MDO2 sample from [34]).

Electron micrographs were collected on some large crystals to assess the layer-to-layer distance. A basal distance of ~11 Å between successive fringes was frequently observed (Fig. 3c) but could rarely be captured, as the crystals vanished under the beam while acquiring micrographs. Crystal damage was systematic during electron diffraction pattern (Fig. 3d). This low stability under the electron beam had already been reported previously [30].

Table 1
Structural parameters derived from EXAFS data simulation.

Atomic pair	*CN*	*R* (Å)	σ^2 (Å^2)[c]	ΔE[d]
Ca–O	4.3[a] ± 1.0	2.36 ± 0.04	0.005 ± 0.003	2.95 ± 2.91
Ca–O	2.7[a] ± 1.0	2.51 ± 0.05	0.005 ± 0.003	2.95 ± 2.91
Ca–Si	1.0[b]	3.11 ± 0.03	0.007 ± 0.002	2.95 ± 2.91
Ca–Si	2.0[b]	3.41 ± 0.03	0.007 ± 0.002	2.95 ± 2.91

Note: Uncertainties are determined with an interactive program for XAFS analysis, the Ifeffit package.

[a] The overall coordination number (*CN*) of Ca–O shells was constrained to 7 as in tobermorite layer.

[b] *CN* of Ca–Si shells were also constrained to the layer crystallographic values in tobermorite.

[c] Debye–Waller factors (σ^2) of the two Ca–O shells and of the two Ca–Si shells were constrained equal.

[d] The variation of the energy threshold (ΔE) was assumed equal for all shells.

3.4. Qualitative description of XRD patterns

All XRD patterns from C–S–H (Fig. 4) display the same number of diffraction maxima, which have similar positions and relative intensities. The only difference between C–S–H XRD patterns is the position and intensity of the ~6.6 °2θ maximum. The presence of these maxima demonstrates that C–S–H are not X-ray amorphous as often assumed but rather hold long range crystallographic order. The similarity between C–S–H XRD patterns indicates also that synthesis temperature has no significant influence on this three-dimensional structure. Comparison with XRD pattern of 11 Å tobermorite, indexed using the tobermorite MDO2 structure model [34], reveals that all diffraction maxima in C–S–H patterns have a position-equivalent maximum in the tobermorite pattern, and mostly correspond to 11 Å tobermorite basal or *hk*0 reflections. The basal tobermorite reflection at ~7.8 °2θ is shifted towards low angles in C–S–H patterns. This suggests for C–S–H a layer structure similar to that of tobermorite, but with turbostratic stacking, that is with the systematic presence of random translations and/or rotations between adjacent layers. In addition, the significant peak broadening, compared to tobermorite, suggests nanometer-sized coherent scattering domains in C–S–H. Nano-crystallinity perpendicular to the layer plane is likely responsible for the low-angle shift of the maximum attributed to the 001 reflection as previously reported for other lamellar structures [48,56–58].

3.5. Simulation of X-ray diffraction pattern

Because EPMA, TEM, and qualitative assessment of XRD patterns consistently indicate strong similarities between studied C–S–H

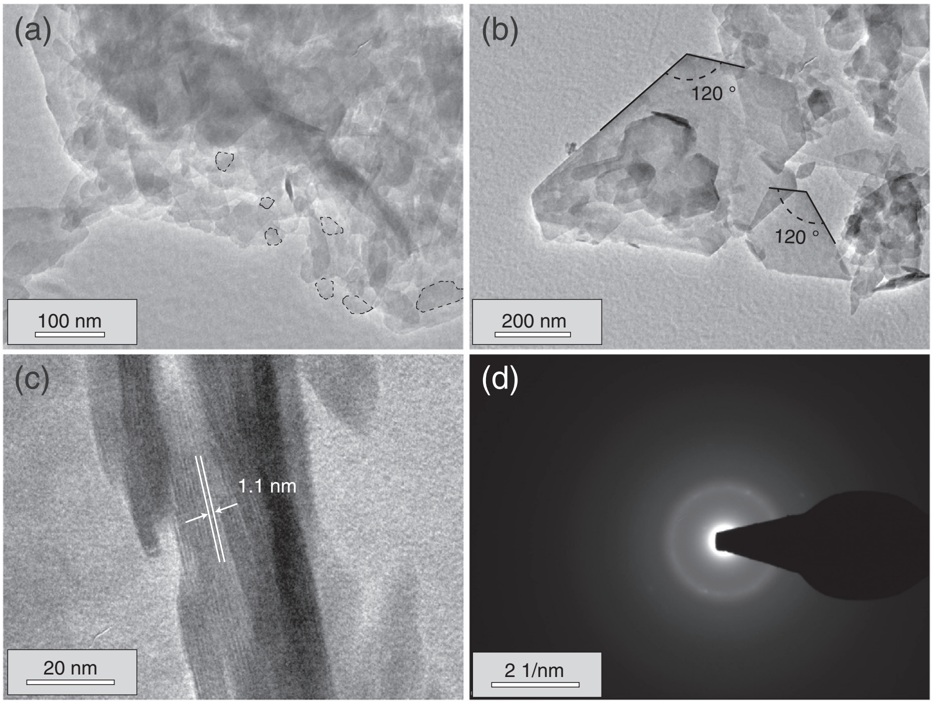

Fig. 3. Selected transmission electron micrographs and diffraction patterns of CSH_RT. Under the beam, C–S–H crystals typically appeared as aggregates of nano-sized and xenomorphic particles (a—dotted line outlines individual crystals), whereas larger crystals, more rarely observed, were automorphic with a typical angle, assumed to be γ, of ~120° (b). Along *c**, interference fringes were separated by ~1.1 nm (c). After a short exposition to the beam, crystals melted yielding amorphous structure, with typical diffraction pattern (d).

and tobermorite, tobermorite structure model [34] was used as a starting model to determine C–S–H structure. As the inclusion of interlayer Ca led to the best simulations (see below), the structure model from sample MDO2 from Urals was preferred. Atomic positions were not refined. The optimum model (R_{wp} = 7.96%, GoF = 4.31), compared to XRD data in Fig. 5, described in Table 2, and schematized in Fig. 6, was obtained from the starting model by reducing the Si content to match the actual Ca/Si ratio and by adjusting crystallite size and **a** and **b** unit-cell parameters. The high sensitivity of calculated XRD patterns to **a** and **b** lattice parameters, distribution of Ca and Si atoms at constant Ca/Si ratio, and crystallite size, both in the **a**–**b** plane and perpendicular to it, are illustrated in Fig. 5. Compared to the starting tobermorite model, **a** and **b** parameters were reduced by 0.25% and 0.80%, respectively. Cell contraction is likely due to C–S–H nano-sized nature, as decreasing particle size increases surface energy and induces lattice contraction [59]. Contraction consistently reduces inter-atomic distances. In the structure model proposed for tobermorite [34], the mean Ca–O distance is 2.46 Å, whereas the distance determined from the present simulation of EXAFS data is equal to (4.3 × 2.36 + 2.7 × 2.51) / 7 = 2.42 Å. To match the measured Ca/Si ratio while achieving optimal simulation quality, the number of Si had to be reduced only in bridging tetrahedra, consistent with previous ^{29}Si NMR studies [19]. C–S–H can thus be described as a nano-crystalline turbostratic tobermorite. The Ca sheets are similar to those of tobermorite, whereas 0.42 Si per bridging tetrahedron site in the dreierketten chains is missing. The mean size of coherent scattering domains is 10 nm within the **a**–**b** plane and crystallites from CSH_RT include 2.8 layers on average. Synthesis temperature has a limited influence on the mean number of stacked layers (CSH_50, CSH_80, and CSH_110 have a mean number of stacked layers of 2.6, 2.6, and 2.9, respectively), contrastingly with the increase in structural disorder occurring when heating air-dried samples to 110 °C [38].

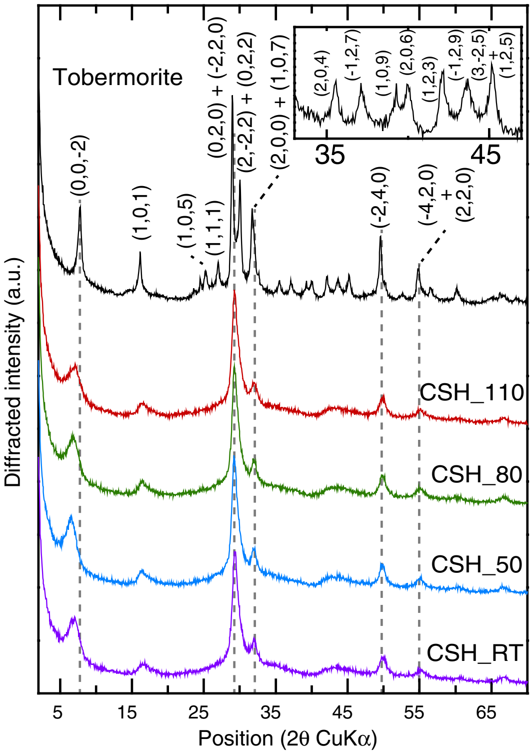

Fig. 4. Qualitative comparison between XRD patterns of synthetic tobermorite, indexed using the MDO2 structure model [34] (top) and CSH_110, CSH_80, CSH_50 and CSH_RT (from top to bottom).

Crystallite size determined from XRD modelling (10 nm) is smaller than crystal sizes observed in the TEM (~10–50 nm). By limiting the observation of the smallest crystals, crystal aggregation may account for part of the discrepancy. In addition, large crystals often appeared curled under the TEM, which likely disrupts the coherency

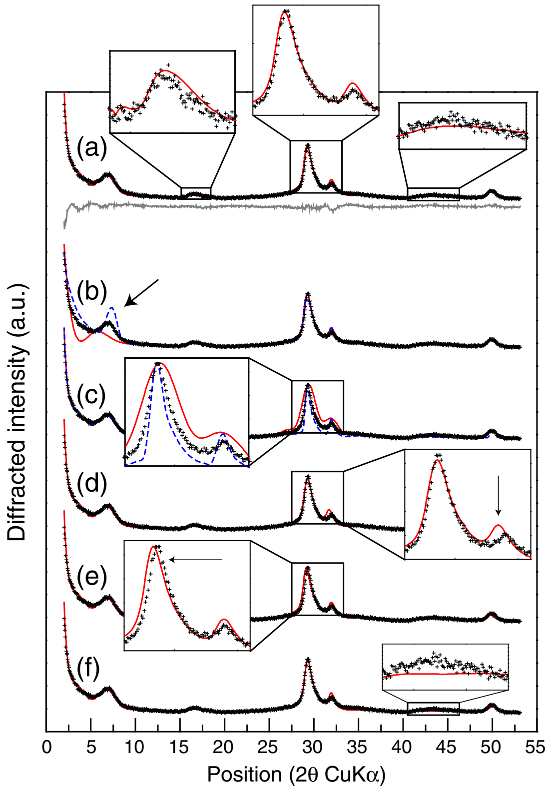

Fig. 5. Simulations of the XRD patterns for CSH_RT. Crosses are experimental points, overplots are calculated profiles, and the solid gray line is the difference plot. (a): Best simulation obtained using structural parameters reported in Table 2. (b): Mean number of layers coherently stacked along c^* reduced to 2 (solid line) or increased to 4 (dotted line), as compared to 2.8 for the optimal structure model (c): Size of the coherent scattering domains within the layer plane reduced to 6 nm (solid line) or increased to 16 nm (dotted line), compared to 10 nm for the optimal model. (d) and (e): **a** and **b** unit-cell parameters, respectively, reduced by 0.05 Å compared to the optimum model. (f): Interlayer calcium omitted and occupation of bridging Si from dreierketten chains reduced to 0.3 yielding the same Ca/Si ratio as in the optimum model. In calculations b to f, detailed views and/or arrows emphasize main discrepancies between experimental and simulations.

of diffracted X-rays within a given particle and thus reduces the apparent crystallite size.

3.6. Implications for mineral nomenclature

Our interpretation of XRD data stands in line with previous structural studies that predicted, from short-range order correspondences, a close similarity between C–S–H with Ca/Si ratio of ~0.8 and tobermorite crystal structures (for more details, the reader is referred to the review article from Richardson [30]) and the presence of structural disorder between successive layers [19]. However, the present study is the first to validate this hypothesis using EXAFS to fit C–S–H spectrum with a tobermorite structure and using powder XRD. In particular, the nature of structural disorder, unit-cell parameters, crystallite size, and relative distribution of Ca and Si cations within the framework were successfully retrieved. C–S–H can be described as nano-crystalline turbostratic tobermorite, with strikingly similar layer and interlayer crystal chemistry, at least when structural Ca/Si ratio is close to that of tobermorite. There is thus no reason to give them a name distinct from tobermorite. Tobermorite can be considered as a suitable analog for C–S–H of equivalent Ca/Si ratio, provided that the drastic decrease in specific surface area, compared to C–S–H, is taken into account. In studied C–S–H, the ratio of external surface to total volume is ~0.06 Å^{-1}, compared to ~0.0002 Å^{-1} for natural tobermorite samples [37]. Our study supports previous reports of C–S–H samples evolution to tobermorite upon aging [60,61]. For the proposed structural analogy, this evolution simply results from a steady improvement of layer stacking.

Table 2
Structural parameters from optimized C–S–H structure model, compared to tobermorite.

Parameter	C–S–H	Tobermorite[a]
a (Å)	6.715	6.732
b (Å)	7.310	7.369
d(001) (Å)	11.34	11.34
γ (°)	123.18[b]	123.18
Occ. bridging Si[c]	0.58	1

Note: All other parameters but unrefined anisotropic displacement factors (set to 1 Å^2 for layer Ca, Si and O from their coordination sphere, and to 2 Å^2 for all other species), including atomic coordinates and site occupancies were set equal to sample tobermorite MDO2 [34].

[a] Sample MDO2 from Urals in [34].

[b] Unrefined parameter.

[c] Site occupancy of bridging Si in dreierketten chains (Si_2 in [34]).

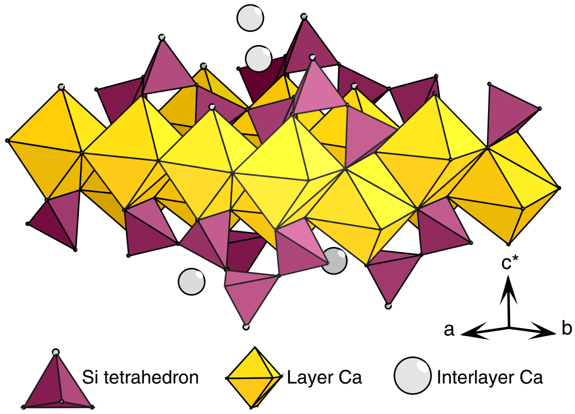

Fig. 6. Sketch of proposed C–S–H structure model. Interlayer water molecules omitted for clarity.

4. Perspectives

The present study reports on the structure of C–S–H present in cement pastes containing for example silica fume or fly ash. Additional data collection and modelling targeting C–S–H samples with higher Ca/Si ratios would be necessary however to determine the crystal structure of C–S–H resulting from the hydration of neat Portland cements. Qualitative observation of XRD patterns from such C–S–H with Ca/Si ratios ranging from ~0.9 to ~1.7 [1] provides some clue on the nature of these phases. They all exhibit *hk*0 reflections at 3.1 Å, 2.8 Å, 1.8 Å and 1.7 Å, typical for turbostratic tobermorite, but inconsistent with jennite, whose most intense *hk*0 reflections occur at 3.47 Å (-310), 3.31 Å (020), and 2.83 Å (120) according to Bonaccorsi and coworkers [62].

The XRD pattern simulation approach used in the present work provides the necessary versatility to assess this hypothesis by fully accounting for the complexity and variability in C–S–H structure. In particular, the XRD patterns from C–S–H may exhibit a modulation at ~30.2 °2θ CuKα [15], corresponding to the most intense *hkl* reflections (2-22 and 022) of tobermorite (Fig. 4), thus suggesting a partially ordered layer stacking. The formalism of Drits and Tchoubar [47] can handle such structural features, and could thus be used for simulation of XRD patterns resembling those of Renaudin and coworkers.

Acknowledgments

This research was funded partly by the ANDRA (French Radioactive Waste Management National Agency) in the framework of the ANDRA/BRGM scientific partnership and by an internal BRGM research project (CARMEN—Caractérisation de la réactivité des minéraux nanocristallins). Synchrotron experiments were performed under the approval of the Photon Factory Program Advisory Committee in High Energy Accelerator Research Organization (KEK: Proposal No. 2009G128). V. Jean-Prost and V. Ruffier are thanked for fruitful discussions. This article benefited from constructive comments and suggestions made by two anonymous reviewers.

References

[1] J.J. Chen, J.J. Thomas, H.F.W. Taylor, H.M. Jennings, Solubility and structure of calcium silicate hydrate, Cem. Concr. Res. 34 (2004) 1499–1519.
[2] H.F.W. Taylor, D.E. Newbury, Calcium hydroxide distribution and calcium silicate hydrate composition in tricalcium silicate and β-dicalcium silicate pastes, Cem. Concr. Res. 14 (1984) 93–98.
[3] H. Manzano, J.S. Dolado, A. Guerrero, A. Ayuela, Mechanical properties of crystalline calcium–silicate–hydrates: comparison with cementitious C–S–H gels, Phys. Status Solidi A 204 (2007) 1775–1780.
[4] I.G. Richardson, G.W. Groves, Microstructure and microanalysis of hardened ordinary Portland cement pastes, J. Mater. Sci. 28 (1993) 265–277.
[5] A. Nonat, The structure and stoichiometry of C–S–H, Cem. Concr. Res. 34 (2004) 1521–1528.
[6] H.F.W. Taylor, Nanostructure of C–S–H: current status, Adv. Cem. Based Mater. 1 (1993) 38–46.
[7] I.G. Richardson, The nature of C–S–H in hardened cements, Cem. Concr. Res. 29 (1999) 1131–1147.
[8] A.V. Girão, I.G. Richardson, R. Taylor, R.M.D. Brydson, Composition, morphology and nanostructure of C–S–H in 70% white Portland cement–30% fly ash blends hydrated at 55 °C, Cem. Concr. Res. 40 (2010) 1350–1359.
[9] C. Plassard, E. Lesniewska, I. Pochard, A. Nonat, Investigation of the surface structure and elastic properties of calcium silicate hydrates at the nanoscale, Ultramicroscopy 100 (2004) 331–338.
[10] M. Atkins, F.P. Glasser, A. Kindness, Cement hydrate phase: solubility at 25 °C, Cem. Concr. Res. 22 (1992) 241–246.
[11] P. Blanc, X. Bourbon, A. Lassin, E.C. Gaucher, Chemical model for cement-based materials: temperature dependence of thermodynamic functions for nanocrystalline and crystalline C–S–H phases, Cem. Concr. Res. 40 (2010) 851–866.
[12] K. Fujii, W. Kondo, Heterogeneous equilibrium of calcium silicate hydrate in water at 30 °C, J. Chem. Soc., Dalton Trans. (1981) 645–651.
[13] S.A. Stronach, F.P. Glasser, Modelling the impact of abundant geochemical components on phase stability and solubility of the $CaO—SiO_2—H_2O$ system at 25 °C: Na^+, K^+, SO_4^{2-}, Cl^- and CO_3^{2-}, Advances in Cement Research, 1997, pp. 167–181.
[14] P. Blanc, A. Lassin, P. Piantone, M. Azaroual, N. Jacquemet, A. Fabbri, E.C. Gaucher, Thermoddem: a geochemical database focused on low temperature water/rock interactions and waste materials, Appl. Geochem. 27 (2012) 2107–2116.
[15] G. Renaudin, J. Russias, F. Leroux, F. Frizon, C. Cau-dit-Coumes, Structural characterization of C–S–H and C–A–S–H samples—part I: long-range order investigated by Rietveld analyses, J. Solid State Chem. 182 (2009) 3312–3319.
[16] G.W. Groves, P.J. Le Sueur, W. Sinclair, Transmission electron microscopy and microanalytical studies of ion-beam-thinned sections of tricalcium silicate paste, J. Am. Ceram. Soc. 69 (1986) 353–356.
[17] P. Yu, R.J. Kirkpatrick, B. Poe, P.F. McMillan, X. Cong, Structure of calcium silicate hydrate (C–S–H): near-, mid-, and far-infrared spectroscopy, J. Am. Ceram. Soc. 82 (1999) 742–748.
[18] R.J. Kirkpatrick, J.L. Yarger, P.F. McMillan, Y. Ping, X. Cong, Raman spectroscopy of C–S–H, tobermorite, and jennite, Adv. Cement Based Mater. 5 (1997) 93–99.
[19] X. Cong, R.J. Kirkpatrick, ^{29}Si MAS NMR study of the structure of calcium silicate hydrate, Adv. Cement Based Mater. 3 (1996) 144–156.
[20] X. Cong, R.J. Kirkpatrick, ^{29}Si and ^{17}O NMR investigation of the structure of some crystalline calcium silicate hydrates, Adv. Cement Based Mater. 3 (1996) 133–143.
[21] G.M. Bowers, R.J. Kirkpatrick, Natural abundance ^{43}Ca NMR spectroscopy of tobermorite and jennite: model compounds for C–S–H, J. Am. Ceram. Soc. 92 (2009) 545–548.
[22] N. Lequeux, A. Morau, S. Philippot, P. Boch, Extended X-ray absorption fine structure investigation of calcium silicate hydrates, J. Am. Ceram. Soc. 82 (1999) 1299–1306.
[23] A.J. Allen, J.J. Thomas, Analysis of C–S–H gel and cement paste by small-angle neutron scattering, Cem. Concr. Res. 37 (2007) 319–324.
[24] A.J. Allen, J.J. Thomas, H.M. Jennings, Composition and density of nanoscale calcium–silicate–hydrate in cement, Nat. Mater. 6 (2007) 311–316.
[25] L.B. Skinner, S.R. Chae, C.J. Benmore, H.R. Wenk, P.J.M. Monteiro, Nanostructure of calcium silicate hydrates in cements, Phys. Rev. Lett. 104 (2010) 195502.
[26] F.P. Glasser, E.E. Lachowski, D.E. Macphee, Compositional model for calcium silicate hydrate (C–S–H) gels, their solubilities, and free energies of formation, J. Am. Ceram. Soc. 70 (1987) 481–485.
[27] A. Nonat, X. Lecoq, The structure, stoichiometry and properties of C–S–H prepared by C_3S hydration under controlled solution, in: P. Colombet, A.-R. Grimmer, H. Zanni, P. Sozzani (Eds.), Nuclear Magnetic Resonance Spectroscopy of Cement Based Materials, Springer, Berlin, 1996, pp. 197–207.
[28] I.G. Richardson, G.W. Groves, Models for the composition and structure of calcium silicate hydrate (C–S–H) gel in hardened tricalcium silicate pastes, Cem. Concr. Res. 22 (1992) 1001–1010.
[29] H.F.W. Taylor, Proposed structure for calcium silicate hydrate gel, J. Am. Ceram. Soc. 69 (1986) 464–467.
[30] I.G. Richardson, The calcium silicate hydrates, Cem. Concr. Res. 38 (2008) 137–158.
[31] E. Bonaccorsi, S. Merlino, A.R. Kampf, The crystal structure of tobermorite 14 Å (plombierite), a C–S–H phase, J. Am. Ceram. Soc. 88 (2005) 505–512.
[32] S. Merlino, E. Bonaccorsi, T. Armbruster, Tobermorites; their real structure and order–disorder (OD) character, Am. Mineral. 84 (1999) 1613–1621.
[33] S. Merlino, E. Bonaccorsi, T. Armbruster, The real structures of clinotobermorite and tobermorite 9 Å, Eur. J. Mineral. 12 (2000) 411–429.
[34] S. Merlino, E. Bonaccorsi, T. Armbruster, The real structure of tobermorite 11 Å, Eur. J. Mineral. 13 (2001) 577–590.
[35] P. Rejmak, J.S. Dolado, M.J. Stott, A. Ayuela, ^{29}Si NMR in cement: a theoretical study on calcium silicate hydrates, J. Phys. Chem. C 116 (2012) 9755–9761.
[36] S. Soyer-Uzun, S.R. Chae, C.J. Benmore, H.-R. Wenk, P.J.M. Monteiro, Compositional evolution of calcium silicate hydrate (C–S–H) structures by total X-ray scattering, J. Am. Ceram. Soc. 95 (2012) 793–798.
[37] T. Maeshima, H. Noma, M. Sakiyama, T. Mitsuda, Natural 1.1 and 1.4 nm tobermorites from Fuka, Okayama, Japan: chemical analysis, cell dimensions, ^{29}Si NMR and thermal behavior, Cem. Concr. Res. 33 (2003) 1515–1523.
[38] X. Cong, R.J. Kirkpatrick, Effects of the temperature and relative humidity on the structure of C–S–H gel, Cem. Concr. Res. 25 (1995) 1237–1245.
[39] T.R. Sweatman, J.V.P. Long, Quantitative electron-probe microanalysis of rock-forming minerals, J. Petrol. 10 (1969) 332–379.
[40] B. Ravel, M. Newville, ATHENA, ARTEMIS, HEPHAESTUS: data analysis for X-ray absorption spectroscopy using IFEFFIT, J. Synchrotron Radiat. 12 (2005) 537–541.
[41] M. Newville, IFEFFIT: interactive XAFS analysis and FEFF fitting, J. Synchrotron Radiat. 8 (2001) 322–324.
[42] B. Ravel, ATOMS: crystallography for the X-ray absorption spectroscopist, J. Synchrotron Radiat. 8 (2001) 314–316.
[43] A.L. Ankudinov, J.J. Rehr, Relativistic calculations of spin-dependent X-ray-absorption spectra, Phys. Rev. B 56 (1997) R1712–R1716.
[44] B.E. Warren, X-ray diffraction in random layer lattices, Phys. Rev. 59 (1941) 693.
[45] A. Plancon, Diffraction by layer structures containing different kinds of layers and stacking faults, J. Appl. Crystallogr. 14 (1981) 300–304.
[46] A. Plancon, CALCIPOW: a program for calculating the diffraction by disordered lamellar structures, J. Appl. Crystallogr. 35 (2002) 377.
[47] V.A. Drits, C. Tchoubar, X-ray Diffraction by Disordered Lamellar Structures: Theory and Applications to Microdivided Silicates and Carbons, Springer-Verlag, Berlin, 1990.
[48] M. Villalobos, B. Lanson, A. Manceau, B. Toner, G. Sposito, Structural model for the biogenic Mn oxide produced by *Pseudomonas putida*, Am. Mineral. 91 (2006) 489–502.
[49] W.P. Gates, P.G. Slade, A. Manceau, B. Lanson, Site occupancies by iron in nontronites, Clays Clay Miner. 50 (2002) 223–239.
[50] S. Grangeon, B. Lanson, M. Lanson, A. Manceau, Crystal structure of Ni-sorbed synthetic vernadite: a powder X-ray diffraction study, Mineral. Mag. 72 (2008) 1279–1291.
[51] S. Grangeon, B. Lanson, N. Miyata, Y. Tani, A. Manceau, Structure of nanocrystalline phyllomanganates produced by freshwater fungi, Am. Mineral. 95 (2010) 1608–1616.
[52] A. Manceau, V.A. Drits, E. Silvester, C. Bartoli, B. Lanson, Structural mechanism of Co^{2+} oxidation by the phyllomanganate buserite, Am. Mineral. 82 (1997) 1150–1175.
[53] S.A. Howard, K.D. Preston, Profile fitting of powder diffraction patterns, Rev. Mineral. Geochem. 20 (1989) 217–275.
[54] E.D. Crozier, A review of the current status of XAFS spectroscopy, Nucl. Instrum. Methods Phys. Res. Sect. B Beam Interact. Mater. Atoms 133 (1997) 134–144.
[55] B.K. Teo, EXAFS: Basic Principles and Data Analysis, Springer, Berlin, 1986.
[56] R. Reynolds Jnr, The effect of particle size on apparent lattice spacings, Acta Crystallogr. Sect. A 24 (1968) 319–320.
[57] V. Trunz, The influence of crystallite size on the apparent basal spacings of kaolinite, Clays Clay Miner. 24 (1976) 84–87.
[58] D.L. Bish, J.E. Post, Modern Powder Diffraction, The Mineralogical Society of America, Washington D.C., 1990
[59] W.H. Qi, M.P. Wang, Y.C. Su, Size effect on the lattice parameters of nanoparticles, J. Mater. Sci. Lett. 21 (2002) 877–878.
[60] T. Mitsuda, H.F.W. Taylor, Influence of aluminium on the conversion of calcium silicate hydrate gels into 11 Å tobermorite at 90 °C and 120 °C, Cem. Concr. Res. 5 (1975) 203–209.
[61] S. Shaw, S.M. Clark, C.M.B. Henderson, Hydrothermal formation of the calcium silicate hydrates, tobermorite ($Ca_5Si_6O_{16}(OH)_2\cdot 4H_2O$) and xonotlite ($Ca_6Si_6O_{17}(OH)_2$): an in situ synchrotron study, Chem. Geol. 167 (2000) 129–140.
[62] E. Bonaccorsi, S. Merlino, H.F.W. Taylor, The crystal structure of jennite, $Ca_9Si_6O_{18}(OH)_6\cdot 8H_2O$, Cem. Concr. Res. 34 (2004) 1481–1488.